

# Tomography of the Solar Corona with Multiple Instruments: First Steps

D.G. Lloveras<sup>1</sup>, A.M. Vázquez<sup>1,2</sup>, E. Landi<sup>3</sup>, & R.A. Frazin<sup>3</sup>

<sup>1</sup> *Instituto de Astronomía y Física del Espacio, CONICET-UBA, Argentina*

<sup>2</sup> *Departamento de Ciencia y Tecnología, UNTREF, Argentina*

<sup>3</sup> *Department of Climate and Space Sciences and Engineering, University of Michigan, USA*

Contact / dlloveras@iafe.uba.ar

**Resumen** / La tomografía solar rotacional es una técnica observacional de la corona solar que permite la reconstrucción de la distribución tridimensional (3D) global de algunos de sus parámetros fundamentales, como por ejemplo la densidad electrónica. La tomografía basada en EUV es aplicada regularmente a datos obtenidos con telescopios espaciales, cubriendo típicamente el rango de alturas heliocéntricas  $1.02 - 1.25 R_{\odot}$ . Este rango solapa parcialmente el del campo de visión del coronógrafo de luz blanca K-coronagraph (KCOR), en el High Altitude Observatory (HAO), que cubre el rango  $1.05 - 3.0 R_{\odot}$ . En este trabajo presentamos resultados preliminares de la primer comparación de una reconstrucción de la densidad electrónica coronal obtenida utilizando imágenes EUV con la obtenida utilizando imágenes en luz blanca. Los resultados obtenidos son discutidos en términos de las diversas características de los datos utilizados, así como de los diferentes factores físicos que afectan cada análisis.

**Abstract** / Solar rotational tomography is an observational technique of the solar corona that allows reconstruction of the global three-dimensional distribution of some of its fundamental physical parameters, such as electron density. EUV tomography is routinely applied to data provided by spaceborne telescopes, typically covering the range of heliocentric heights  $\approx 1.02 - 1.25 R_{\odot}$ . This range partially overlaps that of the field of view of the white light K-coronagraph (KCOR) instrument, at the High Altitude Observatory (HAO), which covers the range  $\approx 1.05 - 3.0 R_{\odot}$ . In this work we show preliminary results of the first comparison of tomographic reconstruction of the coronal electron density based on EUV images against the reconstruction based on white light images. Results are discussed in terms of the diverse characteristics of the used data sets, as well as the different physical factors that affect each analysis.

**Keywords** / Sun: corona — Sun: fundamental parameters — Sun: UV radiation — Sun: abundances

## 1. Introduction

Solar rotational tomography (SRT) was initially developed by Altschuler & Perry (1972) for reconstruction of the three-dimensional (3D) distribution of the coronal electron density based on white light (WL) data. Frazin & Janzen (2002) developed a modern, robust, regularized, positive method for tomographic inversion of the coronal electron density from WL data, used in this work. A thorough review on WL tomography can be found in those references.

More recently, Frazin et al. (2009) developed the differential emission measure tomography (DEMT) technique. DEMT combines EUV tomography in several pass-bands with local DEM analysis, to reconstruct the 3D distribution of both the coronal electron density and temperature. A recent review by Vázquez (2016) summarizes the existing solar physics literature based on DEMT analysis. More recent DEMT-based studies include that by Lloveras et al. (2017), who carried out a comparative analysis of the coronal structure at the solar minima between solar cycles (SC-)22/23 and 23/24.

DEMT research has been carried out based on data provided by several generations of spaceborne EUV telescopes. The latest one is the Atmospheric Imaging As-

sembly (AIA) instrument, on board the Solar Dynamics Observatory (SDO), whose data is used in this work.

While the electron density determined from EUV tomography is dependent on the assumed iron coronal abundance, as well as affected by the so-called coronal filling factor (Frazin et al., 2009), that determined from WL tomography is not (Frazin et al., 2010). So far, no comparison has been carried out between results obtained with both techniques. Here, the tomographic reconstruction of the coronal electron density for a given period is carried out using both methods and their results are compared for the first time.

## 2. Data and Methodology

Carrington rotation (CR-)2198 (from 03 UT 14:37 to 30 UT 22:25 December 2017) was selected as target for analysis, a relatively quiet rotation in the declining activity phase of SC-24. Low latitudes were dominated by the equatorial streamer belt, with a complex of active regions (ARs) located in the longitude range  $\approx 80^{\circ} - 200^{\circ}$ , and high latitudes were dominated by polar coronal holes (CHs).

In this work, tomography is carried out using coronagraph data in the case of KCOR images, and blocking

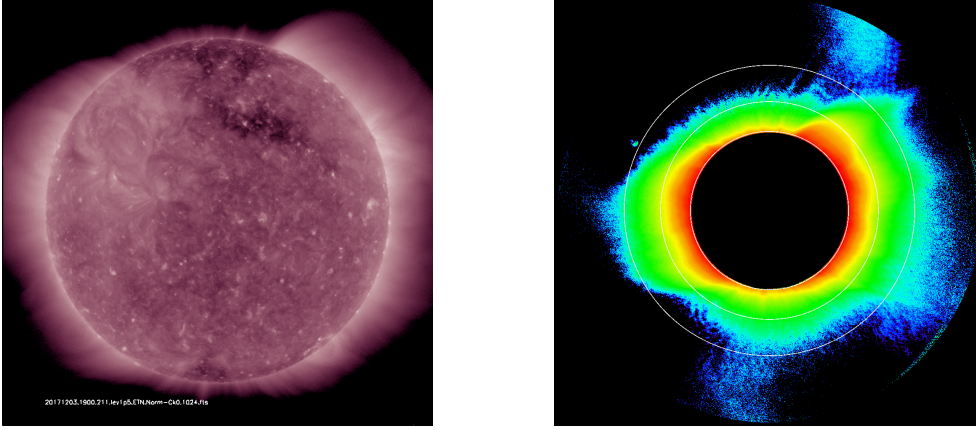


Figure 1: Example of images used for tomographic reconstruction of the coronal electron density of CR-2198 (see text), both corresponding to 2017 December 03 UT 18:00-19:00. Left panel: SDO/AIA coronal EUV image in the 211 Å band. Right panel: HAO/KCOR coronal pB image, with white rings indicating heliocentric heights 1.09, 1.50, and 2.0  $R_{\odot}$ .

the disk in the case of EUV images (i.e. only using off-limb data). As a result, in both cases the data required to provide observations of the corona at all Carrington longitudes is gathered over a lapse equal to half solar synodic rotational period. Specifically, KCOR and AIA images were obtained for the period December 03 through December 17 2017. In the case of AIA, images for all the coronal bands 171, 193, and 211 Å are obtained every 1 hr, and processed with our own tomography data pre-processing tools, which make use of the SolarSoft AIA software in its latest version. In particular, images are averaged over 6 hr long bins, so that a total of about 55 images are used. In the case of KCOR, one 10-minute average coronal polarized brightness (pB) image for each day, obtained using its best observational window, was requested to the instrument team.

Fig. 1 shows examples of the coronal images used for this work. The left panel shows an AIA coronal EUV image taken in its 211 Å band. The right panel shows a KCOR coronal pB WL image. Both images were taken nearly-simultaneously on 2017 December 03 UT 18:00-19:00. This is roughly the beginning of CR-2198, so the longitude of the disk center in these images is  $\approx 0^\circ$ , so the ARs are not seen and the images are dominated by the quiet Sun streamer belt and the CHs.

Both the WL and EUV tomographic reconstructions were performed on the same resolution, with computational voxels having uniform radial size of 0.01  $R_{\odot}$  and angular size of  $2^\circ$  in both latitude and longitude. Solutions were computed with a 3D regularization scheme.

### 3. Results

For the specific data sets of this rotation, the coronal electron density structure was reconstructed in the height range 1.02 – 1.20  $R_{\odot}$  from EUV tomography, and 1.09 – 1.80  $R_{\odot}$  from WL tomography. Fig. 2 shows Carrington maps of both reconstructions at heliocentric height  $r = 1.105 R_{\odot}$ .

The white boxes in the maps indicate two regions selected for quantitative comparison. The region in the Southern hemisphere is a high-density quiet Sun region

within the equatorial streamer belt. The region in the Northern hemisphere is a lower density region at sub-polar latitudes in the northern CH.

The quantitative comparison of the electron density determined from both tomographic analyses at each computational voxel of the two selected regions is shown in Fig. 3. For each region, the top panel shows the histogram of the ratio of electron density as determined from both tomographic analyses for all voxels within the common reconstructed coronal volume, i.e. in the range of heights 1.09 – 1.20  $R_{\odot}$ . For each region, the bottom panel shows the average radial dependence of the electron density determined from both analyses.

### 4. Discussion and Future Work

The coronal electron density determined from WL tomography is systematically larger than that determined from EUV tomography. The characteristic (median) WL-to-EUV electron density ratio is  $\sim 2.0$  in the quiet Sun streamer belt region and  $\sim 1.6$  in the subpolar region within the CH.

This difference may be partly explained by the fact that the KCOR data is affected by the sky brightness which was not subtracted in the specific data set used for this first work, as the required procedures were being revised by the HAO team at the moment of this analysis. Once applied a sky subtraction, the electron density as determined from WL tomography will systematically decrease. If systematic differences persist they can be attributable to physical factors.

Regarding EUV emissivity, firstly, its value determined at each voxel from tomographic analysis is proportional to the local mean squared electron density, i.e.  $E_{\text{EUV}} \propto \langle N_e^2 \rangle = f \langle N_e \rangle^2$ , where the *filling factor* is here defined as  $f \equiv \langle N_e^2 \rangle / \langle N_e \rangle^2 > 1$ . As the WL emission is due to Thompson scattering, its voxel emissivity is proportional to the local average electron density, i.e.  $E_{\text{WL}} \propto \langle N_e \rangle$ . Then:  $\langle N_e \rangle_{\text{WL}} / \langle N_e \rangle_{\text{EUV}} \propto \sqrt{f}$ .

If differences in the results are solely attributed to the filling factor  $f$ , then  $f \sim 4.0$  in the quiet Sun re-



Figure 2: An example of results of the tomographic reconstruction of the coronal electron density for CR-2198. Carrington maps of the reconstructed electron density are shown at heliocentric height  $r = 1.105 R_{\odot}$ . Left panel: reconstruction based on EUV data. Right panel: reconstruction based on WL data. The white boxes indicate two ranges of longitudes and latitudes selected for quantitative comparison (see text).

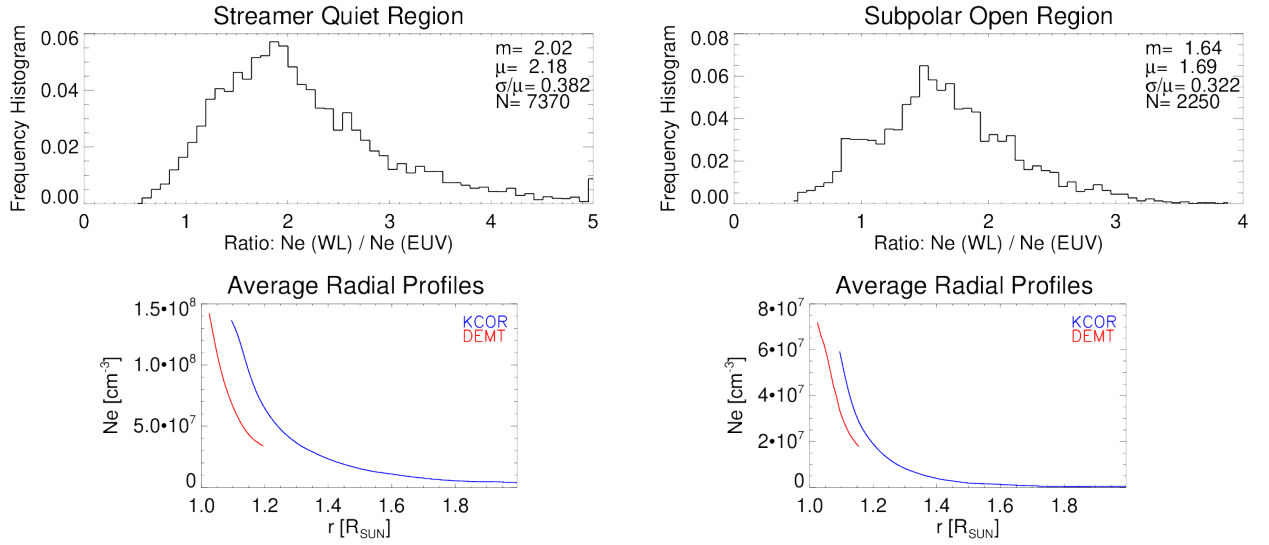


Figure 3: Quantitative comparison between the results of the two tomographic reconstructions of the coronal electron density of CR-2198 in the two selected regions indicated in Fig. 2. Left panels show the results in the quiet Sun region of the southern hemisphere within the streamer belt, and right panels show the results in the subpolar open region within the northern CH. For each region, the top panel shows the histogram of the ratio of the electron density value obtained in each computational voxel from the WL and EUV tomographic analyses. For each region, the bottom panel shows the average radial profile of the electron density based on the EUV (red) and WL (blue) tomographic reconstructions.

gion of the streamer belt, and  $f \sim 2.5$  in the subpolar region of the CH. As for any probability distribution,  $\sigma_{N_e}^2 \equiv \text{Var}(N_e) = \langle N_e^2 \rangle - \langle N_e \rangle^2 = \langle N_e \rangle^2 (f - 1)$ , then  $\sigma_{N_e} / \langle N_e \rangle = \sqrt{f - 1}$ . With this interpretation, where  $f$  is larger (quiet Sun region) the electron density probability distribution has a larger variance.

Secondly, the EUV emissivity determined from tomography is proportional to the assumed iron coronal abundance [Fe]. As a result, the EUV tomography estimate of the average squared electron density scales as  $\langle N_e^2 \rangle \propto 1/[\text{Fe}]$  (Frazin et al., 2009).

The work here summarized is a first step towards development of a new methodology capable of jointly determining the coronal 3D distribution of the electron density and temperature, as well as the filling factor and iron abundance. The technique, dubbed multi-instrument tomography (MIT) and currently under development by us, will involve joint analysis of tomo-

graphic products based on data provided by multiple instruments. These include white-light coronagraphs, EUV telescopes, and visible emission line coronagraphs. In particular, MIT will attempt to combine KCOR, AIA and data from the (soon to be operative) Upgraded Coronal Multichannel Polarimeter (UCoMP) instrument (Landi et al., 2016).

## References

- Altschuler M. D., Perry R. M., 1972, *SoPh*, 23, 410
- Frazin R. A., Janzen P., 2002, *ApJ*, 570, 408
- Frazin R. A., et al., 2010, *SoPh*, 265, 19
- Frazin R. A., Vázquez A. M., Kamalabadi F., 2009, *ApJ*, 701, 547
- Landi E., Habbal S. R., Tomczyk S., 2016, *Journal of Geophysical Research (Space Physics)*, 121, 8237
- Lloveras D. G., et al., 2017, *SoPh*, 292, 153
- Vázquez A. M., 2016, *Advances in Space Research*, 57, 1286

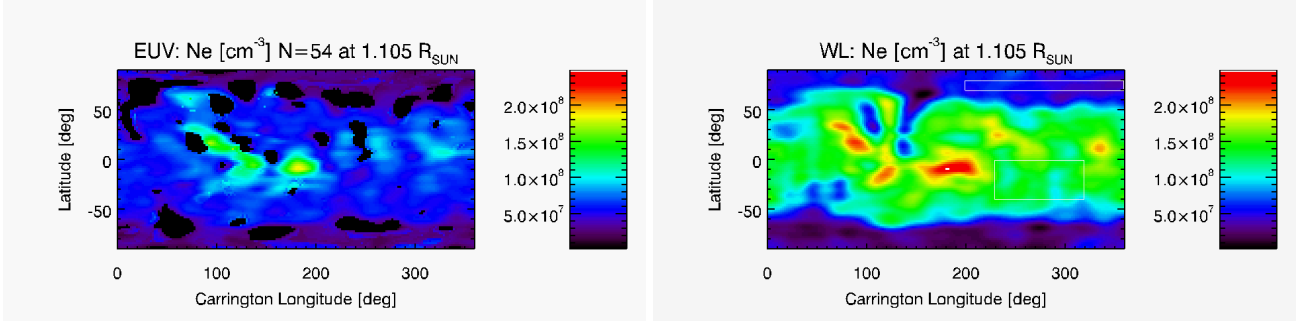


Figure 4: Same as Fig. 2 but with the left panel showing the DENT reconstruction based on EUV images blocked at projected radius  $r < 1.09 R_{\odot}$ , using 4 images per day. Regularization level of DENT is nearly optimal here.

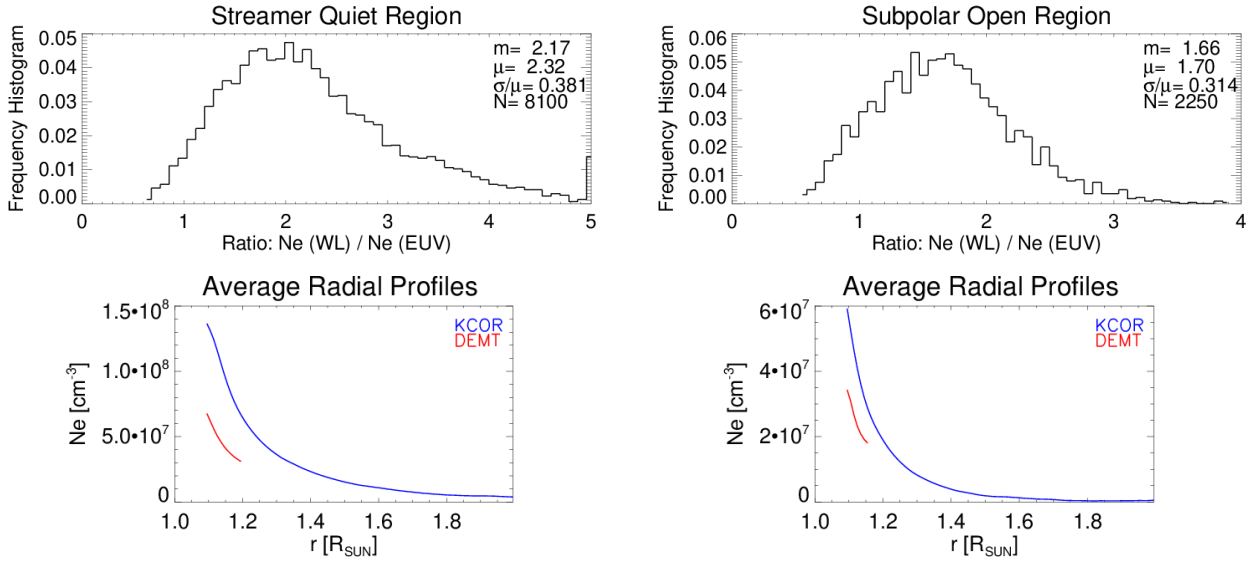


Figure 5: Same analysis of Figure 3, but for the reconstructions shown in Figure 4 above.

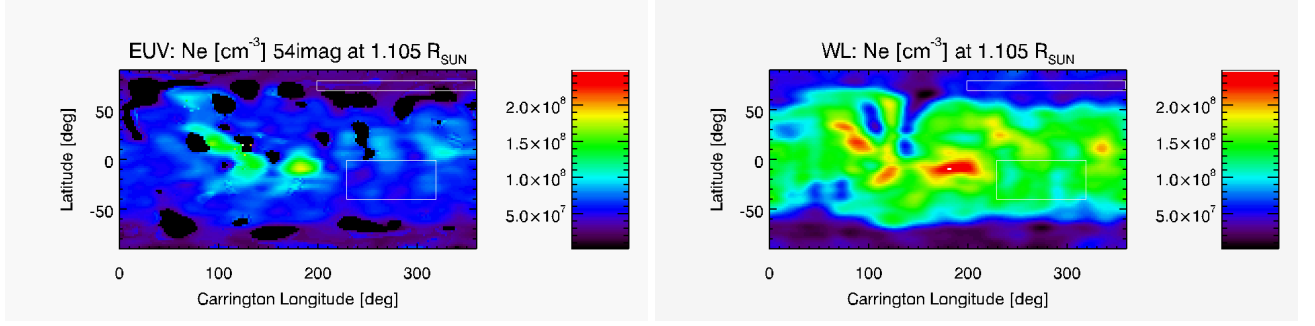


Figure 6: Same as Fig. 2 but with the left panel showing the DENT reconstruction based on EUV images blocked at projected radius  $r < 1.09 R_{\odot}$ , using 4 images per day. Regularization level of DENT is optimal here.

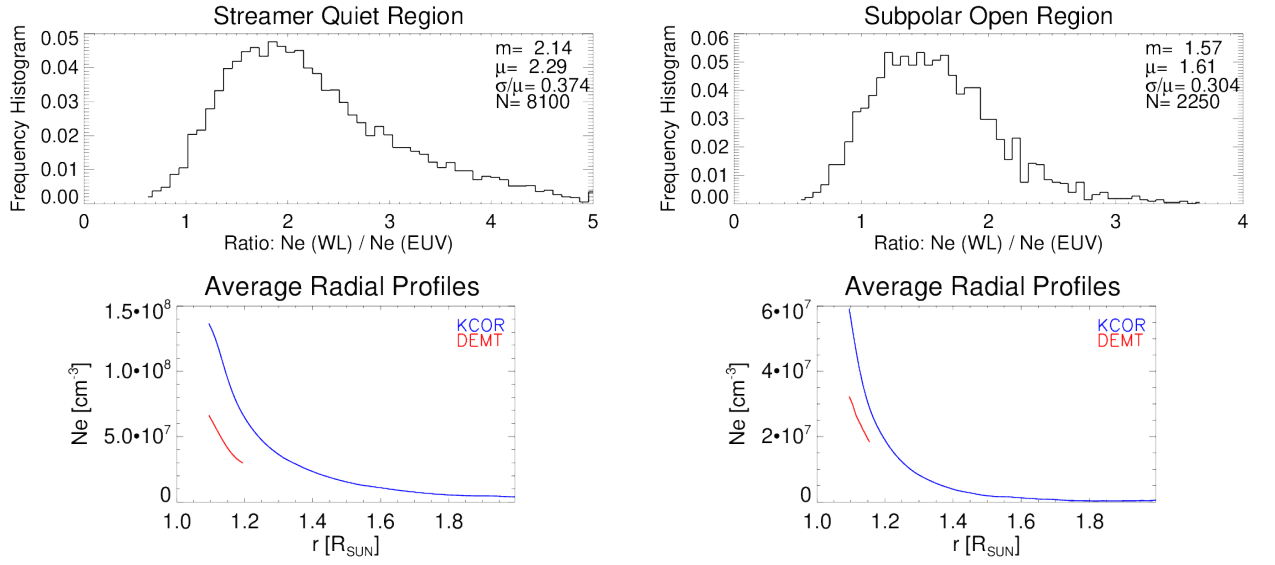


Figure 7: Same analysis of Figure 3, but for the reconstructions shown in Figure 6 above.

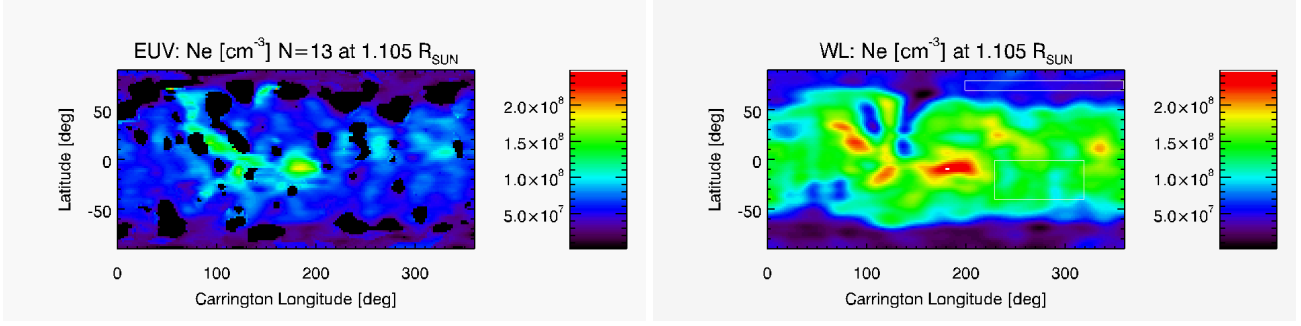


Figure8: Same as Fig. 2 but with the left panel showing the DENT reconstruction based on EUV images blocked at projected radius  $r < 1.09 R_{\odot}$ , using 1 image per day. Regularization level of DENT is far from optimal here.

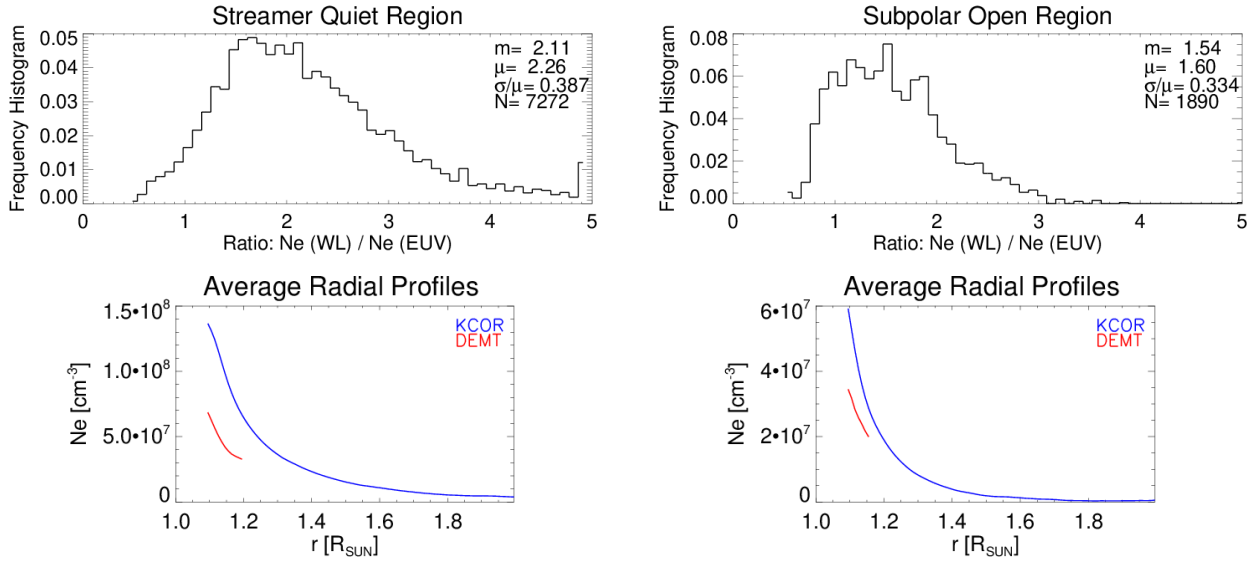


Figure9: Same analysis of Figure 3, but for the reconstructions shown in Figure 8 above.

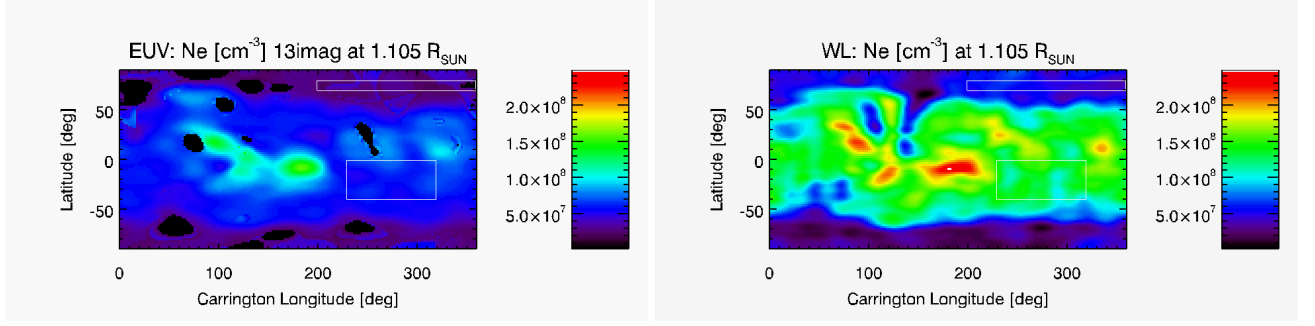


Figure 10: Same as Fig. 2 but with the left panel showing the DGMT reconstruction based on EUV images blocked at projected radius  $r < 1.09 R_{\odot}$ , using 1 image per day. Regularization level of DGMT is optimal here.

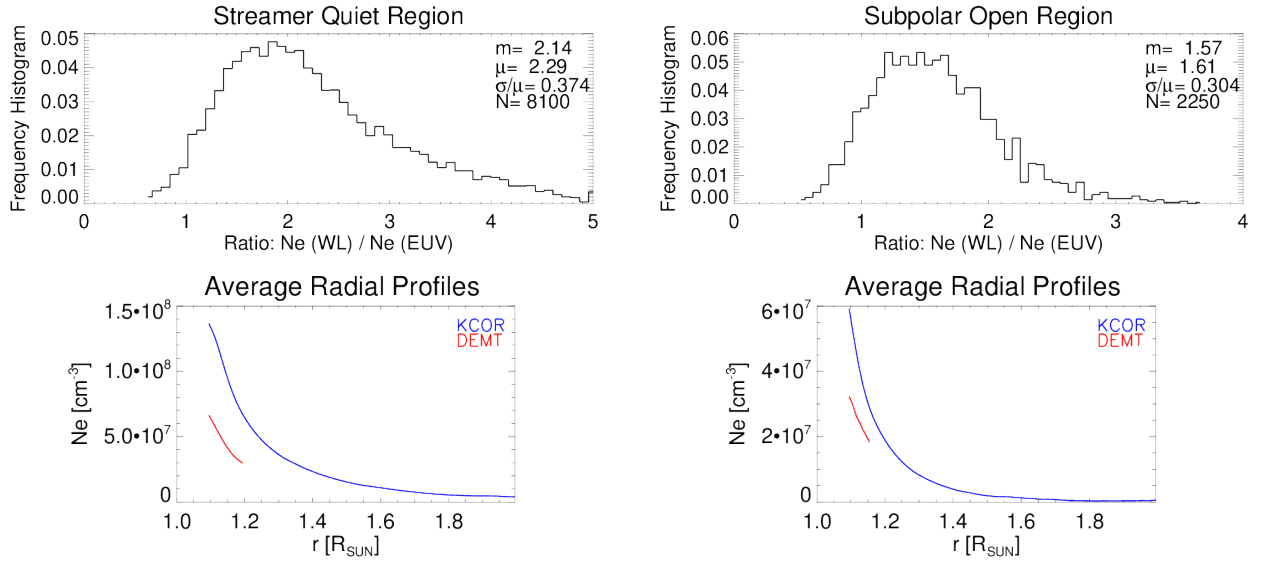


Figure 11: Same analysis of Figure 3, but for the reconstructions shown in Figure 10 above.

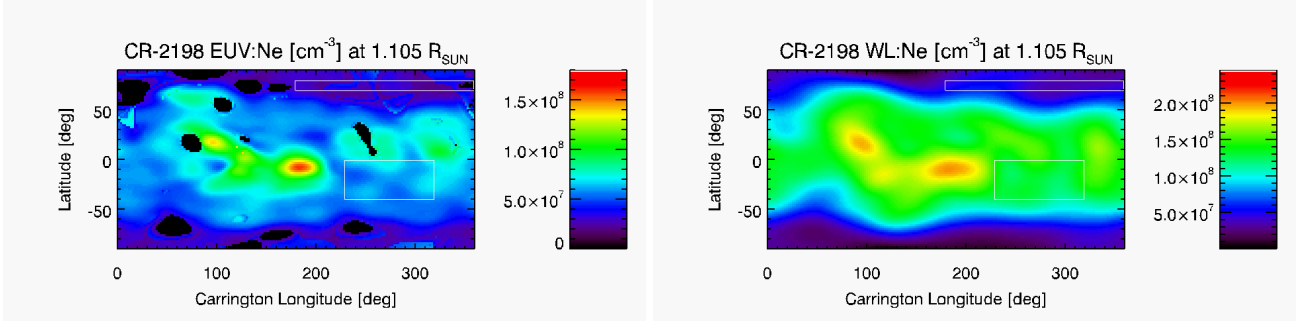


Figure 12: CR-2198: Same as Fig. 2 but with the left panel showing the DENT reconstruction based on EUV images blocked at projected radius  $r < 1.09 R_{\odot}$ , using 1 image per day. Regularization level of DENT is optimal here.

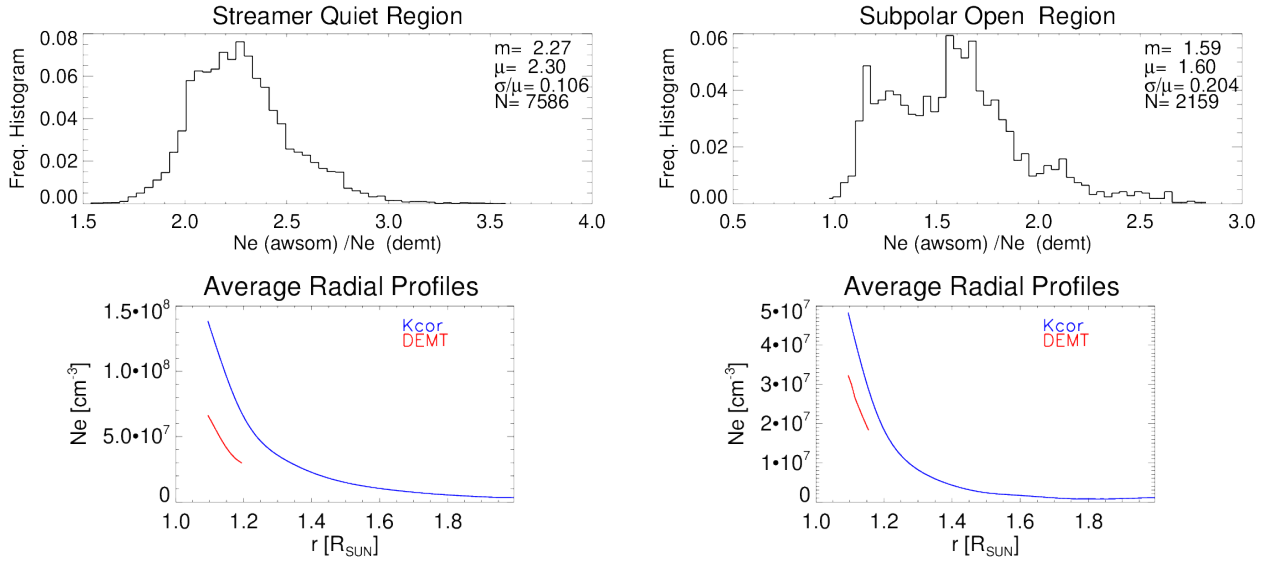


Figure 13: Same analysis of Figure 3, but for the reconstructions shown in Figure 12 above.



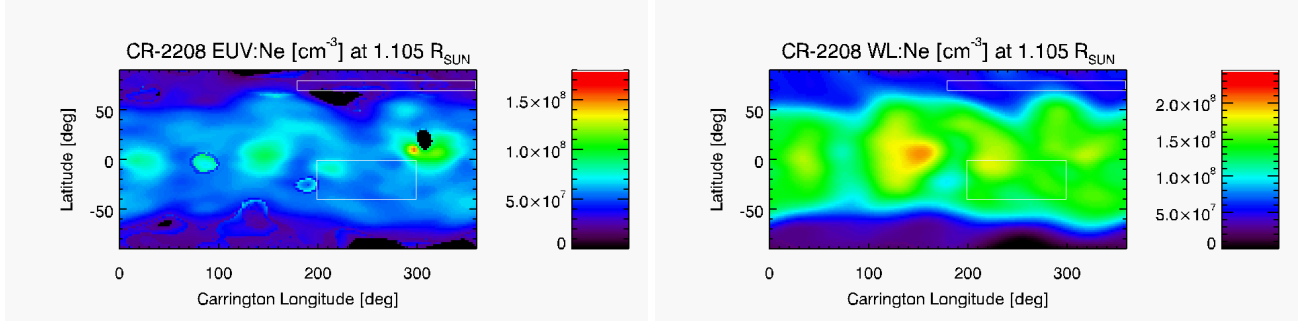


Figure 14: CR-2208: Same as Fig. 2 but with the left panel showing the DENT reconstruction based on EUV images blocked at projected radius  $r < 1.09 R_{\odot}$ , using 1 image per day. Regularization level of DENT is optimal here.

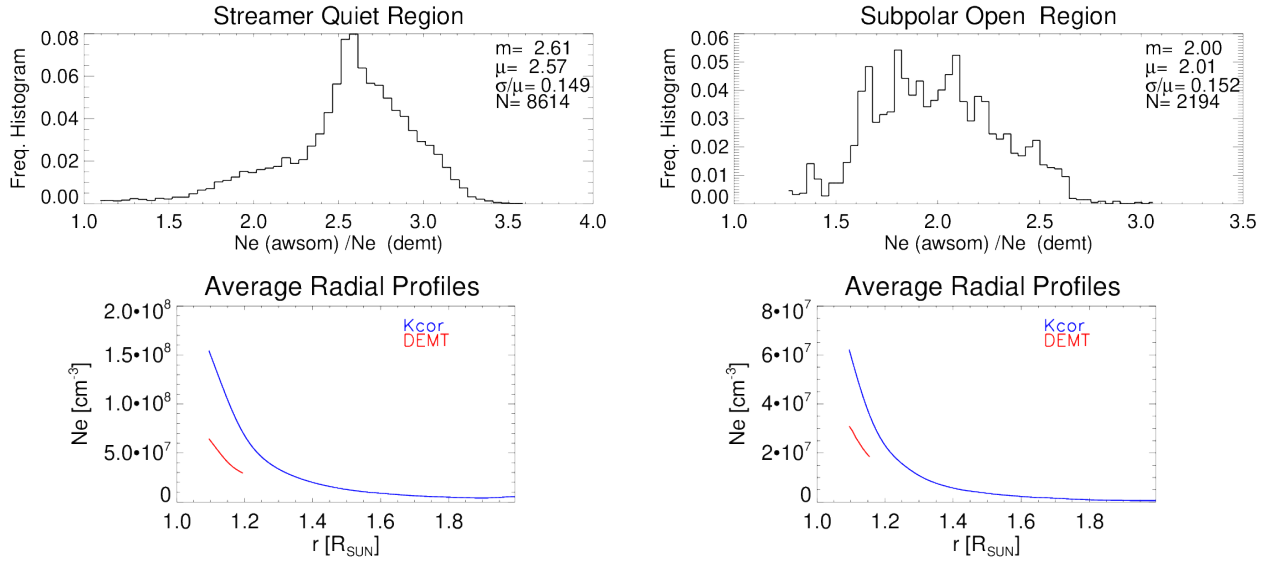


Figure 15: Same analysis of Figure 3, but for the reconstructions shown in Figure 14 above.